**ChemistryOpen**

Research Article
doi.org/10.1002/open.202100296

**Chemistry Europe**
European Chemical Societies Publishing

www.chemistryopen.org

# Amorphous Selenium and Crystalline Selenium Nanorods Graphene Composites as Cathode Materials for All-Solid-State Lithium Selenium Batteries

Han Hu,[a] Fangchao Liu,*[a] Zhongli Shen,[a] Rui Yan,[a] and Zhengwen Fu[b]

Selenium (Se) is an element in the same main group as sulfur and is characterized by high electrical conductivity and large capacity (675 mAh g$^{-1}$). Herein, a novel ultra-high dispersion amorphous selenium graphene composite (a-Se/rGO) was synthesized and a selenium nanorods graphene composite (b-Se/rGO) was prepared by hydrothermal method as the cathode material for all solid-state lithium–selenium (Li–Se) batteries, hoping to improve the efficiency and utilization rate of active substances in all solid-state batteries. The all-solid-state batteries were assembled using a heated thawing electrolyte (2LiI|HPN–LiI; HPN = 3-hydroxypropionitrile). The utilization rate of a-Se/rGO was 103% and the capacity was 697 mAh g$^{-1}$, which remained at 281 mAh g$^{-1}$ (41.6% of the 675 mAh g$^{-1}$) after 30 cycles under 0.5 C. Notably, a-Se/rGO showed excellent performance concerning its utilization rate, with a capacity of up to 610 mAh g$^{-1}$ at 2 C, due to the high availability of amorphous Se and the special properties of the electrolytes. However, in the charge and discharge cycles, the second discharge capacity of a-Se/rGO was more significantly attenuated than that of the first discharge due to the formation of larger crystals of selenium during the charging process. The battery assembled using b-Se/rGO maintained a capacity of 270.58 mAh g$^{-1}$ after 30 cycles (the retention rate of discharge capacity was 66.13% compared with that in the first cycle). Through TEM and other relevant tests, it is speculated that amorphous selenium is conducive to capacity release, which, however, is affected by the formation of crystalline selenium after the first charge process.

## Introduction

With high energy density and long life, lithium ion batteries are widely used in portable electronics, electric vehicles, energy storage equipment and other fields.[1] However, traditional lithium-ion batteries have problems with low energy density, electrolyte leakage and low safety due to flammability.[2] Lithium–sulfur battery a broad application prospect in the field of energy storage because of its high theoretical specific capacity (1675 mAh g$^{-1}$) and energy density (2500 Wh kg$^{-1}$).[3] However, conventional liquid lithium–sulfur batteries have disadvantages such as the insulation of sulfur itself, the shuttle effect of polysulfide and volume change.[4]

In order to solve these problems, all solid state lithium–sulfur batteries have been developing rapidly in recent years.[5] All solid lithium–sulfur batteries can eliminate the shuttle effect of soluble polysulfide compounds, inhibit the growth of lithium dendrites, and overcome the challenges of electrolyte leakage and combustion.[6] However, its practical applications are still limited by solid electrolyte with high hardness, as well as large stress and high interfacial resistance caused by the volume expansion of sulfur.[7] In addition, sulfur has electronic conductivity of $5 \times 10^{-28}$ S m$^{-1}$, which is not conducive to rapid charge transfer and reaction kinetics.[8]

Selenium (Se) is an element in the same main group as sulfur. Compared with sulfur, selenium is conducive to rapid charge transfer and reaction kinetics thanks to its high conductivity ($1 \times 10^{-3}$ S m$^{-1}$).[9] They also have similar reaction mechanism, which can be described as:

$$Se + 2Li^+ + 2e^- \leftrightarrow Li_2Se \tag{1}$$

Based on the above reactions, lithium–selenium battery exhibits a high voltage platform (2.0 V) and a decent weight capacity (675 mAh g$^{-1}$) after complete lithiation.[9–10] Due to high density, selenium still has a high capacity (3260 mAh cm$^{-3}$) despite of its lower weight capacity than sulfur.[11] Therefore, selenium has a potential application prospect in lithium batteries.[12] However, in traditional liquid lithium-ion batteries, similar to sulfur, selenium cathodes exhibit dissolution and multi-selenide shuttle effects (Li$_2$Se$_n$, n > 4), with low utilization rate of active materials and poor cycling performance due to significant volume expansion.[13] On this basis, all solid state lithium–selenium battery is a preferred option to overcome these challenges.

In order to improve reaction kinetics and structural stability, carbon material was used as a conductive matrix to encapsulate

[a]  H. Hu, Dr. F. Liu, Z. Shen, R. Yan
     Shanghai University of Engineering Science
     School of Materials Engineering
     Shanghai (China)
     E-mail: 84309286@qq.com
[b]  Prof. Dr. Z. Fu
     Fudan University
     Shanghai (China)

**ChemistryOpen**

Research Article
doi.org/10.1002/open.202100296

**Chemistry Europe**
European Chemical
Societies Publishing

selenium because of its high electrical conductivity and mechanical strength.[14] With good mechanical properties and special structure, graphene is a favorable material for battery anode.[15] The three-dimensional graphene with high specific surface area are very suitable for fabricating selenium-free electrodes with high uniformity, high dispersion, and flexibility, self-supporting capability without adhesives/conductive agents.[16] In addition, its high conductivity and large specific surface area are conducive to rapid electron transfer and diffusion of lithium ions, which can improve electrochemical reaction kinetics while slowing down volume expansion.[15]

Fan et al.[17] introduced a method of encapsulating hollow selenium in 3D graphene to improve the performance of the positive electrode of lithium selenium battery: Hollow selenium nanospheres encapsulated in 3D graphene hydrogel were prepared by two-step solution method. And the nanocomposite has a certain cyclic stability as a positive electrode (after 50 cycles of 0.2 C, the capacity is 343 mAh g$^{-1}$). The discharge process, the hollow Se@rGO revealed an initial capacity of 543 mAh g$^{-1}$. Zhang et al.[18] designed a graphene-encapsulated selenium/polyaniline core-shell nanowire structure (G@Se/PANI). The Se/PANI core-shell nanowire was uniformly encapsulated in graphene nanosheets. After 200 cycles at 0.2 C and 2 C current densities, the reversible discharge capacities were 567.1 mAh g$^{-1}$ and 510.9 mAh g$^{-1}$, respectively. In addition, Peng et al.[14b] synthesized graphene used the traditional Hummer method and uniformly encapsulated selenium nanoparticles with reduced go (Se@rGO) through a simple self-assembly process. A large initial discharge capacity of 533 mAh g$^{-1}$ at 0.2 C was produced based on the total mass of Se@rGO nanocomposites and the capacity could remain at 265 mAh g$^{-1}$ after 200 cycles at 0.2 C and additional 300 cycles at 1 C. However, all of these Se@rGO as cathode material were liquid electrolytes used in the lithium—selenium batteries.

Herein, amorphous selenium graphene composites (a-Se/rGO) were successfully prepared in the In-situ generated process, and then selenium nanorod graphene composites (b-Se/rGO) was synthesized by hydrothermal method on the basis of a-Se/rGO. The solid electrolyte 2LiI·HPN—LiI is a special type of electrolyte with heat liquefiable property.[19] After liquefaction, it has good infiltration ability for three-dimensional graphene[20] and can provide excellent lithium ion transmission path for highly dispersible selenium on the surface of graphene,[21] which is very suitable for studying new all-solid-state lithium—selenium battery.[6] Furthermore, the mechanism of all-solid-state lithium—selenium battery in charge and discharge process was studied.

## Results and Discussion

Figure 1 shows the X-ray diffraction of elemental Se (PDF.01-073-0465), with a-Se/rGO and b-Se/rGO included for comparison. The XRD patterns of a-Se/rGO show a wide peak at $2\theta = 24°$, corresponding to the diffraction of the (002) planes of graphene.[22] Compared with selenium elemental substance, selenium has no obvious diffraction in a-Se/rGO samples, which
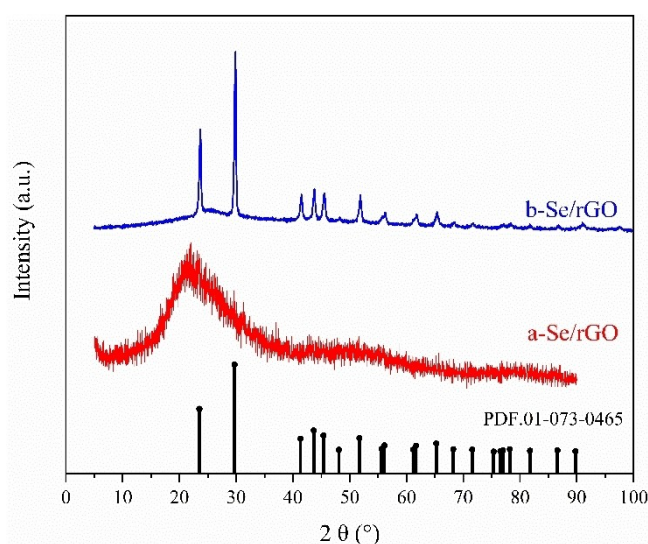


**Figure 1.** XRD patterns of a-Se/rGO (red), b-Se/rGO (blue) and Se (PDF.01-073-0465).

indicates that the selenium produced by in situ synthesis reaction in the sample is an amorphous structure.[23] However, selenium has obvious diffraction in b-Se/rGO samples, consistent with standard PDF.01-073-0465 cards for selenium, suggesting that the b-Se/rGO prepared by hydrothermal method is selenium nanorods.

Figure 2a shows the Raman spectra of a-Se/rGO and b-Se/rGO composite materials. It can be seen from the figure that both a-Se/rGO and b-Se/rGO composite materials have two peaks: One (D-band) is located at 1340.5 cm$^{-1}$ (disorder caused by sp$^3$ defect), and the other (G-band) at 1584.8 cm$^{-1}$ (sp$^2$ bond pair). In addition, the intensity ratio of D/G band ($I_D/I_G$) varies with the change of carbon structure. The higher the strength ratio of D/G band intensity, the worse the electron conductivity.[7] The $I_D/I_G$ of a-Se/rGO composite was greater than that of b-Se/rGO, indicating that the electronic conductivity of a-Se/rGO composite was lower than that of b-Se/rGO. This is because the interlayer structure of graphene is changed by selenium nanorods inserted in the middle of graphene, indicating that the electrical conductivity of the composite is further improved when selenium nanorods are combined with three-dimensional graphene. The selenium loading in the electrode was measured by thermogravimetric analysis in the nitrogen atmosphere, TGA curves of a-Se/rGO as shown in Figure 2b. Selenium has weight loss at about 320–480 °C due to sublimation of selenium, which indicates that graphene contains about 48% selenium in a-Se/rGO, almost identical to 43% selenium added in the initial experiment. TGA curves of b-Se/rGO as shown in Figure S2, which indicates that graphene contains about 46.4% selenium in b-Se/rGO, a small amount of selenium loss may be caused by the hydrothermal process.

Figure 2c shows XPS wide spectra of a-Se/rGO and b-Se/rGO. Both of them consist of C, O, and Se. The peaks at about 190, 161, and 56 eV can be respectively assigned to Se 3 s, 3p, and 3d signals.[24] The signal intensity of Se for a-Se/rGO
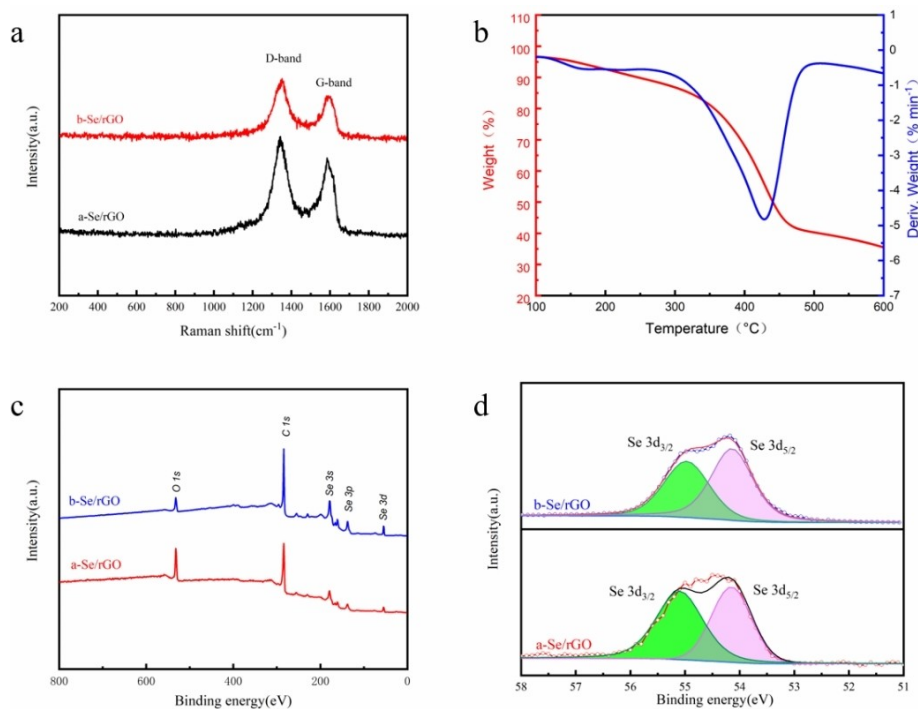
**ChemistryOpen**

Research Article
doi.org/10.1002/open.202100296

**Chemistry Europe**
European Chemical
Societies Publishing

**Figure 2.** (a) Raman spectrum of a-Se/rGO (black) and b-Se/rGO (red); (b) TGA curves of a-Se/rGO; (c) wide XPS and (d) high-resolution XPS spectra of the Se 3d with peak fitting analysis.

demonstrates that selenium was successfully compounded into graphene, whose signal, however, was not reflected in XRD due to high dispersion. The high-resolution XPS of Se is shown in Figure 2d. The doublet at binding energies of 55.1 and 54.15 eV are respectively attributed to the Se 3d3/2 and Se 3d5/2 of a-Se/rGO.[24b] By comparison, the positions of the Se in b-Se/rGO 3d3/2 and 3d5/2 shift to 54.97 and 54.14 eV, respectively, which is possibly associated with the interaction between Se molecules and rGO.[25]

In contrast, the morphology of a-Se/rGO is displayed in Figure 3a–d. It is the structural property of graphene itself, with orderly distributed holes on the surface, and Se microparticles in the a-Se/rGO mixture disappear in the in situ synthesis reaction process, which shows that selenium and graphene have been perfectly combined. The three-dimensional porous structure of the composite electrode can facilitate the liquefied electrolyte to completely infiltrate the electrode, and the cross-linked structure forms a good conductive network, which greatly improves the conductivity of the composite electrode. Figure 3e–f presents the EDS mapping results for C and Se in the a-Se/rGO composite electrode, respectively. It can be seen from the figure that selenium is uniformly dispersed on the graphene sheets, which further illustrates that selenium is highly dispersed with an amorphous state on the surface of the graphene. Figure 3g–h shows the back scattering electron (BSE) imaging of a-Se/rGO. It can be seen from the figure that amorphous selenium is evenly distributed on graphene, which is consistent with the result of EDS mapping. It is also worth noting that amorphous selenium can provide high selenium

utilization during electrochemical lithiation, as can be seen from the first discharge capacity of the battery.

According to the SEM figure, there is no selenium particle in the graphene, and Se is uniformly distributed, as can be seen from the EDS mapping. $Li_2Se$ is speculated to be formed after the first discharge. TEM images of lithium selenide electrode after charging are shown in Figure 4. After the first charge, rod-like selenium formation can be seen in the graphene, with a length of about 2.5 μm and a diameter of about 1.6 μm, as displayed in Figure 4a. As Figure 4b shows, it is (210), (201), (112) and (031), which is characteristic diffraction of selenium from the diffraction spots, implying that amorphous selenium changes from amorphous to stable crystal in the discharging and recharging processes. According to the TEM of a-Se/rGO after charging and the electrochemical performance of a-Se/rGO in the cycling process, selenium nanorods graphene composite materials (b-Se/rGO) were designed and prepared to verify that the crystal selenium is disadvantage to battery discharge.

The morphology of b-Se/rGO is displayed in Figure 5a–d. As can be seen from the figure, selenium nanorods are interspersed with graphene and are pierced from graphene. This is because the amorphous selenium gradually forms the selenium nanorods during the hydrothermal process, followed by gradual growth. Selenium nanorods are interspersed between each layer of graphene, greatly improving the conductivity of the composite electrode. According to the figure, the cross section of selenium nanorods is hexahedron, which is related to the crystal configuration of selenium. Figure 5e–g presents the EDS mapping results for Se and C in the b-Se/rGO composite
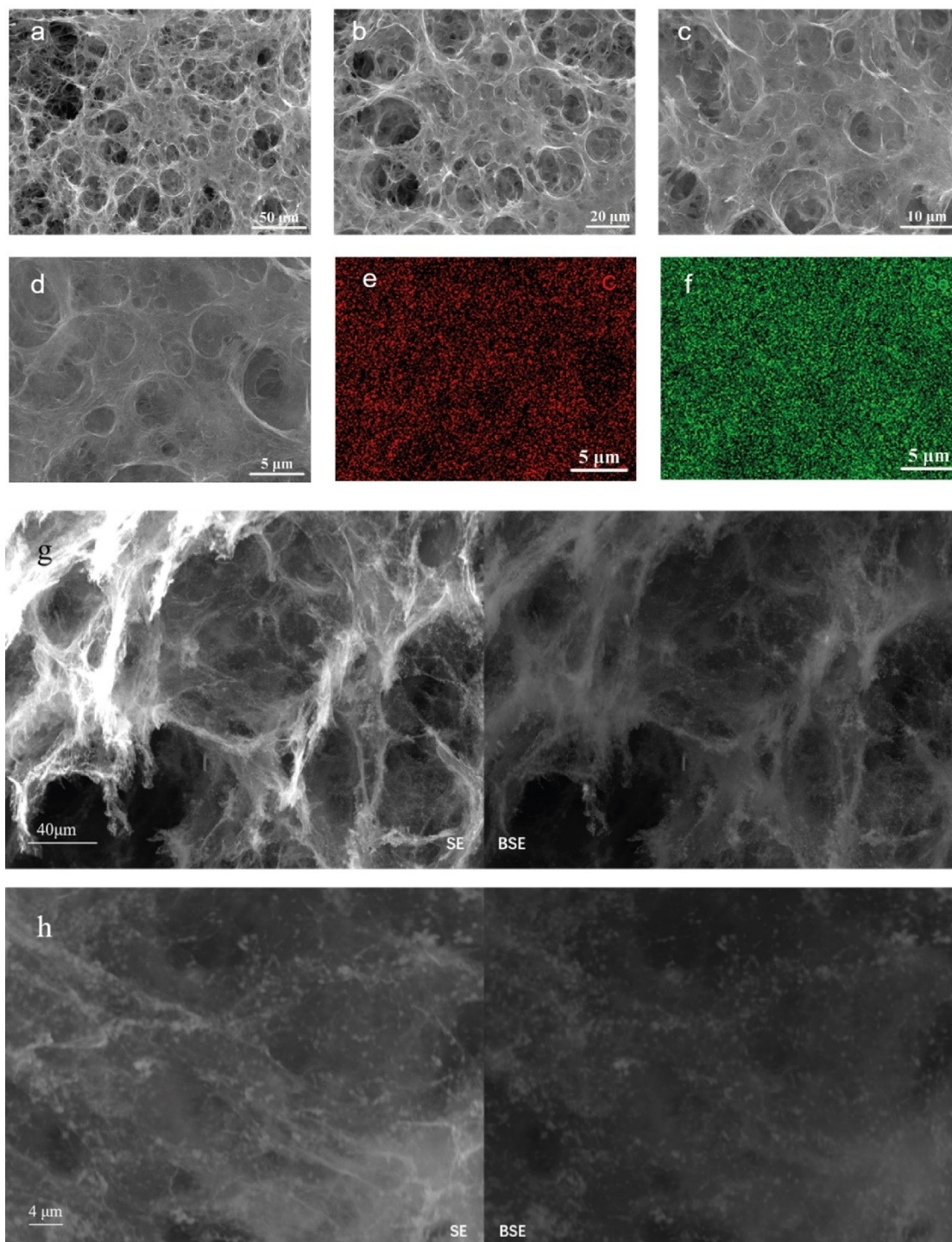
ChemistryOpen

Research Article
doi.org/10.1002/open.202100296

Chemistry
Europe
European Chemical
Societies Publishing

**Figure 3.** (a–d) SEM and (e–f) EDS mapping (g–h) SE and BSE of the a-Se/rGO composite material.

electrode, respectively. Selenium nanorods can be seen interspersed with graphene, which further illustrates the structure of selenium nanorods in graphene.

The electrochemical performances of two different composite electrodes were investigated using all-solid-state cell of Li/2LiIHPN–LiI/2LiIHPN–LiI@ES. The open circuit voltage of the battery was 2.7 V, and the galvanostatic charge and discharge were performed using 2LiIHPN–LiI solid electrolyte. The

discharge curves of the Li/2LiIHPN–LiI/2LiIHPN–LiI@a-Se/rGO battery at different discharge current densities are shown in Figure 6a. The battery was discharged at the current densities of 2, 1, 0.5, 0.25, 0.10 and 0.05 C, and their discharge capacity is 610, 645, 697, 746, 772 and 792 mAh g$^{-1}$ (675 mAh g$^{-1}$, Se), respectively. It is observed that at a current density of 2 C, the discharge capacity of the battery is as high as 90% of the theoretical specific capacity. However, at the current densities
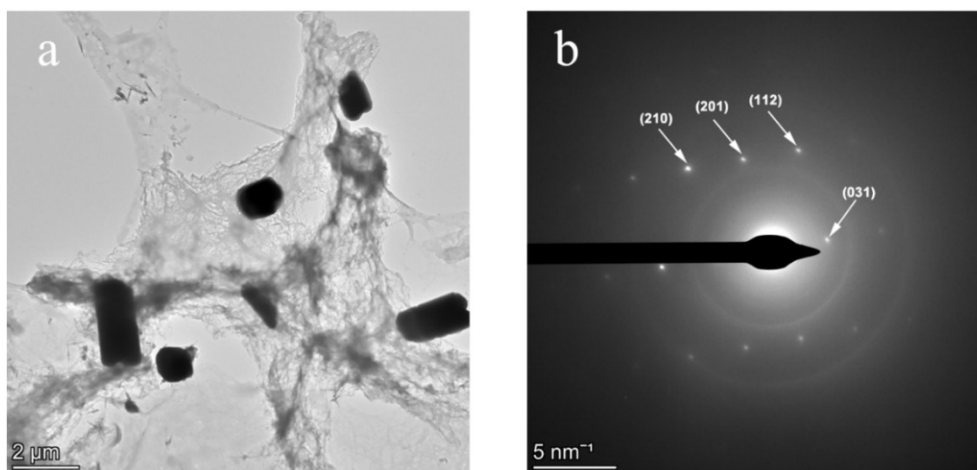
**ChemistryOpen**

Research Article
doi.org/10.1002/open.202100296

**Chemistry
Europe**
European Chemical
Societies Publishing

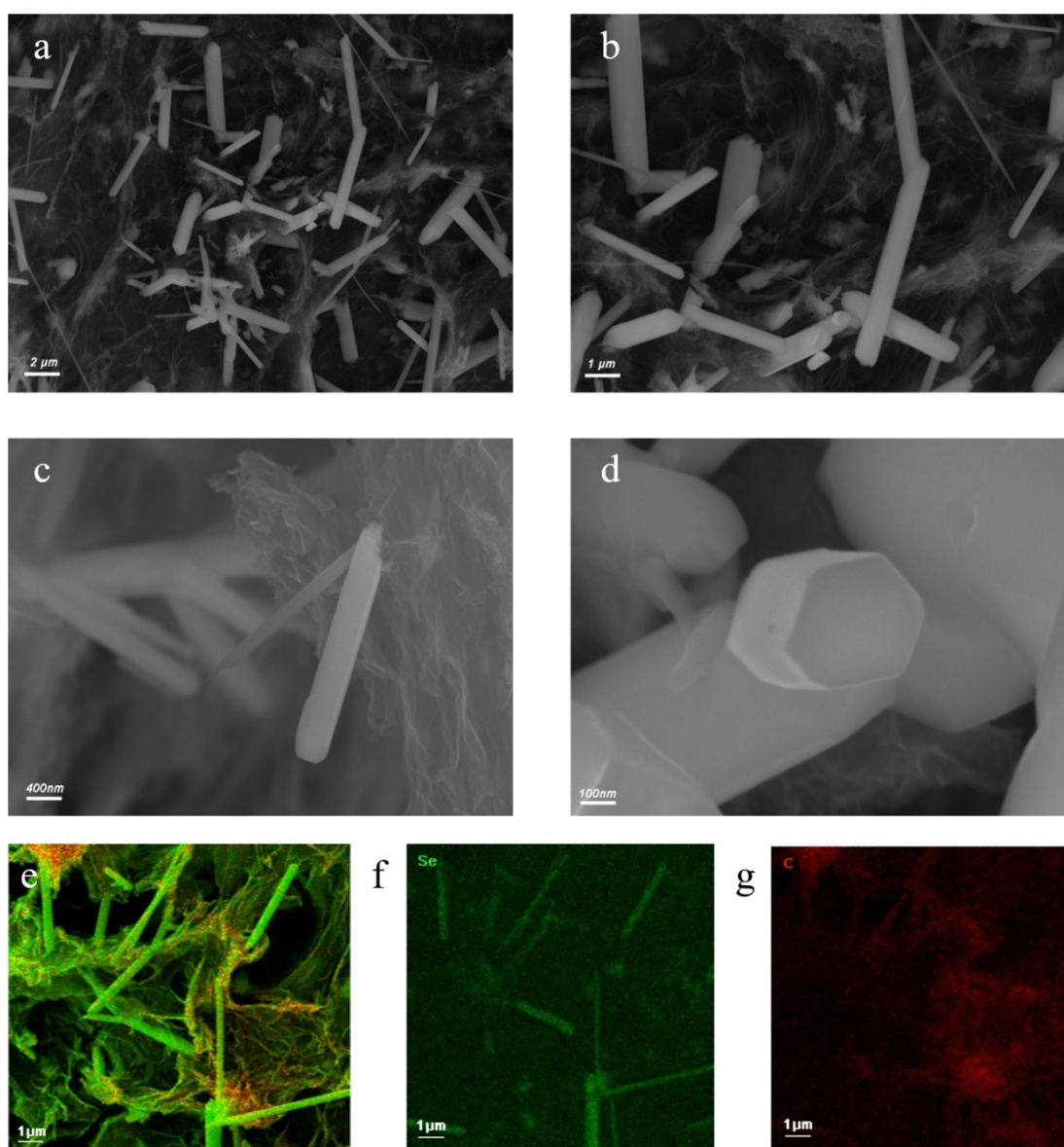**Figure 4.** (a) TEM image after the first cycle, (b)SAED of the a-Se/rGO composite material.



**Figure 5.** (a–d) SEM micrographs at different magnifications and (e–g) EDS mapping of the a-Se/rGO composite material.
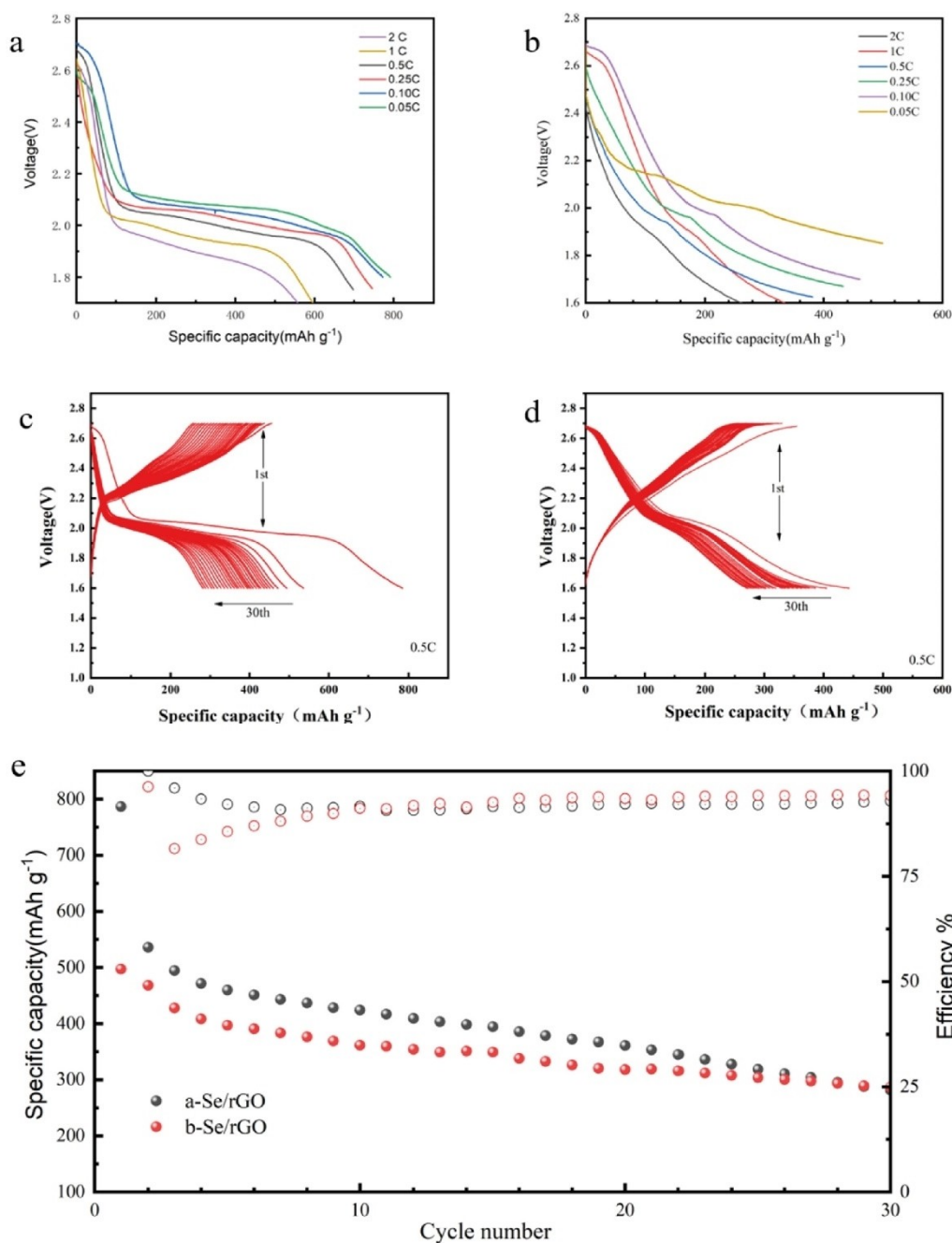
**Figure 6.** Rate-dependent characterization of the assembled a-Se/rGO (a) and b-Se/rGO (b) batteries; different cycle performance of the assembled a-Se/rGO (c) and b-Se/rGO (d) batteries at 0.5 C; (e) discharge capacity and efficiency comparison.

of 0.5, 0.10 and 0.05 C, the initial discharge capacity of the battery is higher than the theoretical specific capacity of selenium, which may be due to the contribution of the capacity of the 2LiIHPN–LiI electrolyte at low current densities. Figure 6c shows the initial 30 cycles of galvanostatic discharge-charge profiles of the a-Se/rGO in all-solid-state Li–Se battery under 0.5 C, and with cutoff voltages of 1.6 V and 2.7 V. During the second discharge, the capacity is reduced to 68.17 % of the initial discharge capacity. The average discharge and charge voltage platform is in the range of 1.9–2.1 V and 2.2–2.5 V. This is different from traditional Li/Se cells in organic liquid electro-

lytes, which typically exhibit one obvious discharge platform, depending on the reaction mechanism. The discharge curves of the Li/2LiIHPN–LiI/2LiIHPN–LiI@b-Se/rGO batteries at different discharge current densities are shown in Figure 6b. The batteries were discharged at the current densities of 2, 1, 0.5, 0.25, 0.10 and 0.05 C, and their discharge capacity is 258.55, 334.6, 380.2, 432.5, 460.7 and 499.5 mAh g$^{-1}$, respectively. Figure 6d shows the initial 30 cycles of galvanostatic discharge-charge profiles of the b-Se/rGO in all-solid-state Li–Se battery under 0.5 C, and with cutoff voltages of 1.6 V and 2.7 V. the first discharge capacity was 441.17 mAh g$^{-1}$, and the capacity

**ChemistryOpen**

Research Article
doi.org/10.1002/open.202100296

**Chemistry**
**Europe**
European Chemical
Societies Publishing

remained at 270.58 mAh g$^{-1}$ (The retention rate of discharge capacity was 66.13% compared with the first time) after 30 cycles. The average discharge and charge voltage platform is in the range of 1.9–2.1 V and 2.2–2.5 V, respectively, which is consistent with the result of a-Se/rGO.

The CV curves of batteries with different electrode assemblies were measured. As illustrated in Figure 7a, there are two reduction peaks at 1.978 V and 2.015 V in the CV curve of a-Se/rGO assembled battery which matches with the discharge curve, corresponding to the first discharge process of selenium. There are two obvious oxidation peaks at 2.24 V and 2.479 V, corresponding to the processes of Li$_2$Se charging and generating Se. The reduction peak at about 2.0 V corresponds to the platform of the discharge curve, which might be related to the reaction of 2Li + Se → Li$_2$Se, and the oxidation peak at about 2.5 V also corresponds to the platform of the charging curve that might related to the reaction of Li$_2$Se → 2Li + Se. As exhibited in Figure 7b, there is one reduction peak at 1.961 V in the CV curve of b-Se/rGO assembled battery, which matches with the discharge curve, corresponding to the first discharge process of selenium. There is an obvious oxidation peak at 2.251 V, with small peak current.

EIS analysis can be used to study the attenuation and reaction mechanism of lithium–selenium battery as it can effectively provide the change of battery resistance and discharge condition. The EIS of all-solid-state Li–Se battery by a-Se/rGO at a current density of 0.5 C, before discharge and after 30 cycles is shown in Figure 7c. Through fitting, before discharge, the value of electrolyte/electrode (Rs) is 113.48 Ω and that of electrolyte charge transfer (Rct) is 146.6 Ω; after 30 cycles, the value of Rs is 151.78 Ω and that of Rct is 133.7 Ω. Figure 7d shows the EIS of all-solid-state Li–Se battery by b-Se/rGO at a current density of 0.5 C before discharge and after 30 cycles. Through fitting, before discharge, the values of Rs and Rct are 115.41 Ω and 101.6 Ω; after 30 cycles, they are 186.78 Ω and 209.3 Ω, which indicates after the cycle, the interfacial resistance increases, while the charge transfer increases to a certain extent. This may be because after multiple discharges,
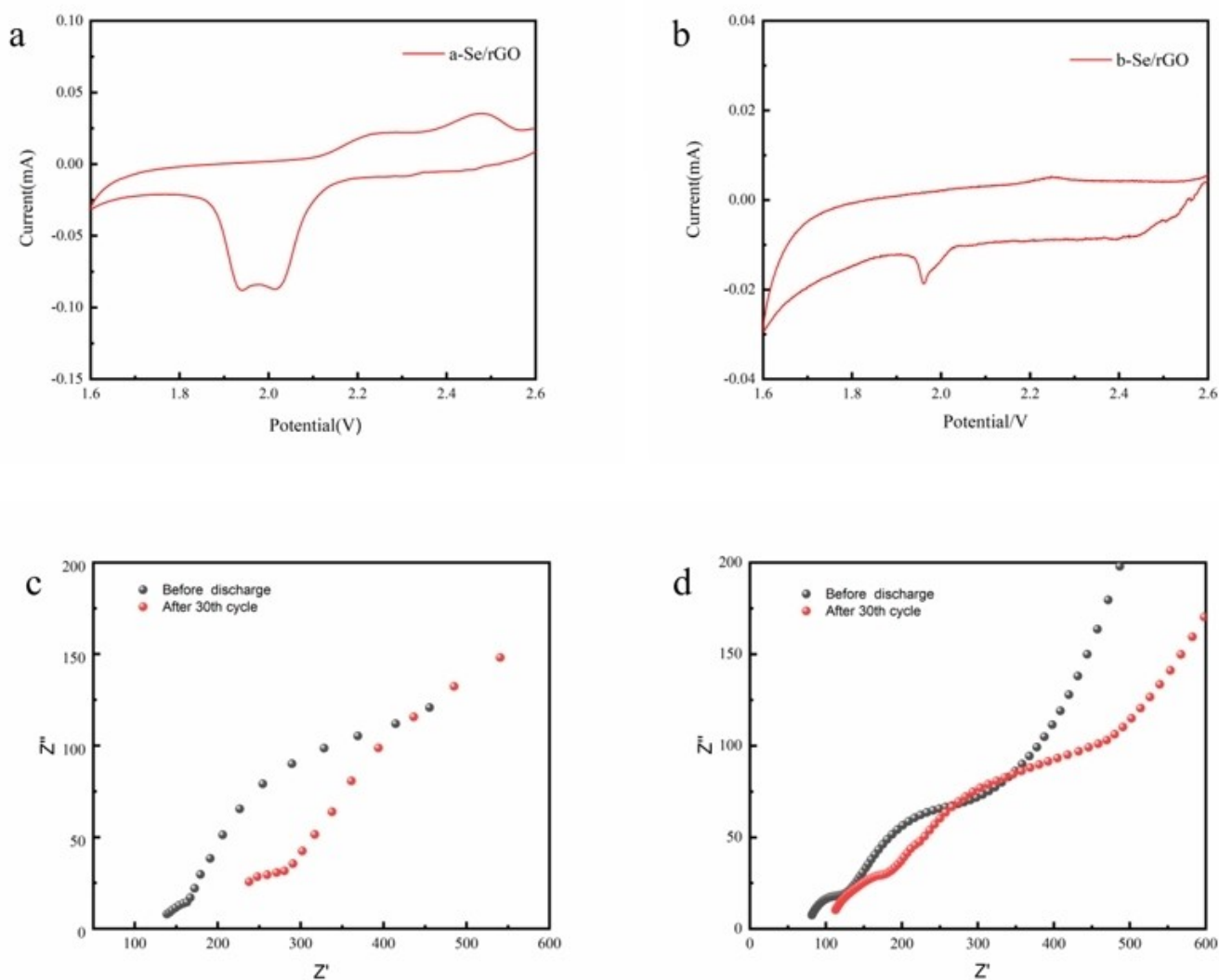


**Figure 7.** (a–b) Different battery CV curves at the sweep speed of 0.05 mV s$^{-1}$. EIS spectra before cycling and after the 30th cycle of the (c) a-Se/rGO assembled battery and the (d) b-Se/rGO assembled battery.

**ChemistryOpen**

Research Article
doi.org/10.1002/open.202100296

**Chemistry**
**Europe**
European Chemical
Societies Publishing

the elemental grains of selenium become larger and the interfacial resistance increases to a certain extent.

Obviously, in the charge and discharge cycle, the second discharge capacity of a-Se/rGO witnesses a greater attenuation than that the first discharge Through TEM and other related tests, it can be hypothesized that amorphous selenium is conducive to capacity release, which, however, is affected by amorphous selenium forms rod-like selenium after the first charge. The performance tests of the prepared selenium nanorods graphene composite materials also confirm the above assumption.

## Conclusion

A selenium graphene composite electrode with high dispersion was successfully prepared by the in situ growth method, and selenium nanorods graphene composite materials were fabricated by the hydrothermal method. The discharge and charge product of the a-Se/rGO cathode under 0.5 C condition was analyzed by SEM and TEM, and the reaction mechanism of $Li_2Se \leftrightarrow Se$ was determined. In addition, relevant tests for the prepared selenium nanorods graphene composite materials have verified that amorphous selenium is conducive to while crystalline selenium is unfavorable for the overall capacity of the system. We have for the first time observed the charging products of all-solid-state Li—Se batteries. Due to amorphous selenium, Se demonstrates high activity at the first discharge. The Li—Se battery shows a high 2 C performance of 610 mAh g$^{-1}$, and the utilization rate of Se reaches 100% at 0.5 C. Further research on this material in the cycle of all-solid-state battery has certain significance for the further development of all-solid-state-batteries.

## Experimental Section

**Materials**: Graphite was purchased from Sinopharm Chemical Reagent Co., Ltd. Potassium nitrate ($KNO_3$), sodium selenite ($Na_2SeO_3$), lithium iodide (LiI), concentrated sulfuric acid ($H_2SO_4$), concentrated hydrochloric acid (HCl) and potassium permanganate ($KMnO_4$) were purchased from Shanghai Titan Co., Ltd. Ascorbic acid (Vc) and lithium tablets were purchased from Afa Aisa (China) Chemical Co., Ltd. 3-Hydroxypropionitrile (HPN) was purchased from Aladdin Reagents Co., Ltd. Ultrapure water (18.2 MΩ cm) was used in all of experiments.

**Preparation of the Solid-State Electrodes**: The solid electrolyte 2LiIHPN—LiI is prepared from HPN and the highly pure LiI crystal. LiI and HPN were proportionally mixed at 25 °C and then stirred at 120 °C for 24 h to obtain a homogeneous liquid in an anhydrous glove box. The obtained solid electrolyte is directly used to assemble an all-solid-state lithium—selenium battery under heating conditions.

**Amorphous Selenium Graphene Composite (a-Se/rGO) and Selenium Nanorod Graphene Composites (b-Se/rGO) Electrode Sheet**: GO (Graphene oxide) was synthesized from graphite powder by Hummers' method,[26] obtaining a GO suspension(3 mg mL$^{-1}$). a-Se/rGO is prepared by in situ synthesis with Vc as the reducing agent. $Na_2SeO_3$(0.125 g) was added to deionized water(10 mL) to

form a solution of 0.07 mmol/ml, $Na_2SeO_3$ solution(2 mL) was added to the GO(5 mL) suspension with vigorous stirring, get a mixed solution. Vc(1.6 mg) was added to deionized water(10 mL) to form a solution of 0.9 mmol/ml, Vc solution(2 mL) was added to the mixture. Then, taking the same volume(0.22 mL) of the mixture onto the slide and the dropped slide was placed in an oven at 110 °C for 75 minutes. The obtained three-dimensional graphene foam selenium electrode sheet was washed with deionized water to remove excess impurities, and then the wet electrode sheet are freeze dried for 24 h to obtained a-Se/rGO composite electrode. b-Se/rGO material was synthesized by prepared a-Se/rGO, which was put into a reaction kettle with deionized water as solution, heated at 150 °C and kept for 24 h, and then the wet electrode sheet are freeze dried for 24 h to obtained b-Se/rGO composite electrode. the composite diagram is shown in Figure S1 The prepared composite electrode is a round sheet that can be used directly without the need for adhesives and conductive agents.

## Conflict of Interest

The authors declare no conflict of interest.

## Data Availability Statement

The data that support the findings of this study are openly available in Han Hu at https://doi.org/[doi], reference number 32.

[1] a) A. Abouimrane, D. Dambournet, K. W. Chapman, P. J. Chupas, W. Weng, K. Amine, *J. Am. Chem. Soc.* **2012**, *134*, 4505–4508; b) F. Sun, H. Cheng, J. Chen, N. Zheng, Y. Li, J. Shi, *ACS Nano* **2016**, *10*, 8289–8298; c) X. Li, J. Liang, J. Luo, C. Wang, X. Li, Q. Sun, R. Li, L. Zhang, R. Yang, S. Lu, H. Huang, X. Sun, *Adv. Mater.* **2019**, *31*, e1808100.

[2] a) N. Ohta, K. Takada, L. Zhang, R. Ma, M. Osada, T. Sasaki, *Adv. Mater.* **2006**, *18*, 2226–2229; b) M. Nagao, Y. Imade, H. Narisawa, T. Kobayashi, R. Watanabe, T. Yokoi, T. Tatsumi, R. Kanno, *J. Power Sources* **2013**, *222*, 237–242; c) X. Han, Y. Gong, K. K. Fu, X. He, G. T. Hitz, J. Dai, A. Pearse, B. Liu, H. Wang, G. Rubloff, Y. Mo, V. Thangadurai, E. D. Wachsman, L. Hu, *Nat. Mater.* **2017**, *16*, 572–579.

[3] a) P. G. Bruce, S. A. Freunberger, L. J. Hardwick, J.-M. Tarascon, *Nat. Mater.* **2012**, *11*, 19–29; b) Y.-X. Song, Y. Shi, J. Wan, S.-Y. Lang, X.-C. Hu, H.-J. Yan, B. Liu, Y.-G. Guo, R. Wen, L.-J. Wan, *Energy Environ. Sci.* **2019**, *12*, 2496–2506.

[4] a) Y.-X. Yin, S. Xin, Y.-G. Guo, L.-J. Wan, *Angew. Chem. Int. Ed.* **2013**, *52*, 13186–13200; *Angew. Chem.* **2013**, *125*, 13426–13441; b) M. Nagao, A. Hayashi, M. Tatsumisago, *J. Mater. Chem.* **2012**, *22*.

[5] A. Manthiram, X. W. Yu, S. F. Wang, *Nat. Rev. Mater.* **2017**, *2*, 16.

[6] R. Zhu, F. Liu, W. Li, Z. Fu, *ChemistrySelect* **2020**, *5*, 9701–9708.

[7] X. Yao, N. Huang, F. Han, Q. Zhang, H. Wan, J. P. Mwizerwa, C. Wang, X. Xu, *Adv. Energy Mater.* **2017**, *7*.

[8] F. Han, J. Yue, X. Fan, T. Gao, C. Luo, Z. Ma, L. Suo, C. Wang, *Nano Lett.* **2016**, *16*, 4521–4527.

[9] Q. Zhang, L. Cai, G. Liu, Q. Li, M. Jiang, X. Yao, *ACS Appl. Mater. Interfaces* **2020**, *12*, 16541–16547.

[10] C.-P. Yang, Y.-X. Yin, Y.-G. Guo, *J. Phys. Chem. Lett.* **2015**, *6*, 256–266.

[11] H. Ye, Y.-X. Yin, S.-F. Zhang, Y.-G. Guo, *J. Mater. Chem. A* **2014**, *2*, 13293–13298.

[12] C.-P. Yang, S. Xin, Y.-X. Yin, H. Ye, J. Zhang, Y.-G. Guo, *Angew. Chem. Int. Ed.* **2013**, *52*, 8363–8367; *Angew. Chem.* **2013**, *125*, 8521–8525.

[13] J. Jin, X. Tian, N. Srikanth, L. B. Kong, K. Zhou, *J. Mater. Chem. A* **2017**, *5*, 10110–10126.

[14] a) J. B. Goodenough, K. S. Park, *J. Am. Chem. Soc.* **2013**, *135*, 1167–1176; b) X. Peng, L. Wang, X. Zhang, B. Gao, J. Fu, S. Xiao, K. Huo, P. K. Chu, *J. Power Sources* **2015**, *288*, 214–220.

[15] X. Huang, X. Qi, F. Boey, H. Zhang, *Chem. Soc. Rev.* **2012**, *41*, 666–686.

[16] M. F. El-Kady, V. Strong, S. Dubin, R. B. Kaner, *Science* **2012**, *335*, 1326–1330.

[17] S. Fan, Y. Zhang, S.-H. Li, T.-Y. Lan, J.-L. Xu, *RSC Adv.* **2017**, *7*, 21281–21286.

[18] J. Zhang, Y. Xu, L. Fan, Y. Zhu, J. Liang, Y. Qian, *Nano Energy* **2015**, *13*, 592–600.

[19] F.-C. Liu, Z. Shadike, F. Ding, L. Sang, Z.-W. Fu, *J. Power Sources* **2015**, *274*, 280–285.

[20] F.-C. Liu, W.-M. Liu, M.-H. Zhan, Z.-W. Fu, H. Li, *Energy Environ. Sci.* **2011**, *4*.

[21] F. C. Liu, Z. Shadike, X. F. Wang, S. Q. Shi, Y. N. Zhou, G. Y. Chen, X. Q. Yang, L. H. Weng, J. T. Zhao, Z. W. Fu, *Inorg. Chem.* **2016**, *55*, 6504–6510.

[22] X. Chen, L. Peng, L. Wang, J. Yang, Z. Hao, J. Xiang, K. Yuan, Y. Huang, B. Shan, L. Yuan, J. Xie, *Nat. Commun.* **2019**, *10*, 1021.

[23] J. Zhang, Q. Fu, Y. Xue, Z. Cui, *CrystEngComm* **2018**, *20*, 1220–1231.

[24] a) C. Zheng, M. Liu, W. Chen, L. Zeng, M. Wei, *J. Mater. Chem. A* **2016**, *4*, 13646–13651; b) C. Wang, Q. Hu, Y. Wei, D. Fang, W. Xu, Z. Luo, *Ionics* **2017**, *23*, 3571–3579.

[25] H. Ye, Y.-X. Yin, S.-F. Zhang, Y.-G. Guo, *J. Mater. Chem. A* **2014**, *2*.

[26] C. Luo, Y. Xu, Y. Zhu, Y. Liu, S. Zheng, Y. Liu, A. Langrock, C. Wang, *ACS Nano* **2013**, *7*, 8003–8010.